# On the prediction of the yield stress of unimodal and multimodal $\gamma'$ Nickel–base superalloys

E.I. Galindo-Nava[1,*], L.D. Connor[2] and C.M.F. Rae[1]

[1]Department of Materials Science and Metallurgy, University of Cambridge

27 Charles Babbage Rd, Cambridge, CB3 0FS, UK

[2] Diamond Light Source, Harwell Science and Innovation Campus, Didcot, OX11 0DE, UK

*email: eg375@cam.ac.uk, +44 1223 334300

**Abstract**

A new model for the yield stress in superalloys accounting for unimodal and multimodal $\gamma'$ size distributions is presented. A critique of the classic models on $\gamma'$ shearing is presented and important features not previously considered are incorporated in our model. This is extended to account for multimodal particle size distribution effects by weighting the individual particle contribution to the total strength. This analysis is focused on powder metallurgy alloys. The yield stress and particle strengthening are predicted for eight superalloys containing wide variations in initial microstructure, composition and at temperatures up to 700 °C. We demonstrate through a theoretical approach that the strength of alloys with multimodal $\gamma'$ is lower than those with unimodal $\gamma'$ radius in the vicinity of 10–30 nm. For the first time, a parameter–free physics–based model is able to predict the yield stress in superalloys with complex microstructures, including unimodal and multimodal $\gamma'$ size. This has been possible by removing limitations inherent to the classical models. Such approach also enables critical evaluation of the relevant factors contributing to the yield strength of polycrystalline superalloys.

Keywords: Nickel; superalloys; yield strength; precipitation hardening; deformation

## 1 Introduction

Polycrystalline nickel–base superalloys are employed in high–temperature structural components in aircraft engines and power generation turbines. These alloys typically possess microstructures consisting of a face–centred cubic matrix ($\gamma$), and can contain multimodal size distributions of $L1_2$ precipitates ($\gamma'$), the primary $\gamma'$ which is 1–5 $\mu$m in size and is

located on the $\gamma$ grain boundaries*, and two populations of intragranular particles of secondary $\gamma'$ of 50–300 nm in radii and tertiary $\gamma'$ of 2–50 nm in radii. These complex distributions allow superalloys to reach high yield strengths ($\geq$ 1 GPa) at temperatures up to 750 °C, whilst displaying high creep and fatigue life properties [1]. Primary $\gamma'$ acts to limit grain growth during solution treatment and enhances grain boundary strengthening. Tertiary $\gamma'$ particles are known to increase creep life by controlling the mechanisms of dislocation dissociation and decreasing dislocation mobility to reduce the strain rate [2]; additionally, the crack growth rate increases for larger secondary $\gamma'$ particles [3]. Time dependent crack growth is also very sensitive to the size of tertiary $\gamma$', with much reduced crack growth rates for larger tertiary sizes compared to those for fine tertiary $\gamma$' [4]; this is attributed to reduced crack tip stresses as a result of more stress relaxation in coarse tertiary $\gamma$' material. Additionally, Collins and Stone [5] have shown experimentally in RR1000 that unimodal distributions of very fine $\gamma'$ particles are stronger than multimodal $\gamma'$ distributions of the same volume fraction; however, the ductility dropped dramatically to 2 % in the former, whereas for the latter elongation is typically in the range of 12–25 % [5,6]. These results confirm that multimodal $\gamma'$ distributions are more desirable to ensure a wider range of optimal mechanical properties.

It is well established that $\gamma'$ shearing is the main contributor to the strength of polycrystalline superalloys and modelling the individual contributions of each $\gamma'$ size range must be considered. This deformation process has been the subject of theoretical studies for over 50 years [7–13], where quantitative insights on the interactions between dislocation pairs with small (weak pair–coupling) and large (strong pair–coupling) $\gamma'$ particles have been obtained; however, these results are restricted to alloys with unimodal particle size distributions and low volume fractions. This also reflects the fact that there is a limited number of physics–based modelling approaches in superalloys with multimodal $\gamma'$, as one would expect to predict the strength of wide range of particle sizes and volume fractions in excess of 45 % [1]. For instance, Kozar *et al.* [14], have proposed a model including multimodal $\gamma'$ size effects by partially modifying the weak pair–coupling

*No primary $\gamma'$ is present for heat treatments above the $\gamma$' solvus temperature allowing grain growth.

mechanism and introducing size distributions effects in the tertiary $\gamma'$; although good predictions were obtained for subsolvus heat–treatment conditions (fine grain and low tertiary $\gamma'$ volume fraction), their model displayed opposite strengthening effects under supersolvus conditions (coarse grain and higher tertiary $\gamma'$ volume fraction); these results indicate that their model is not correctly sensitive to variations in the $\gamma'$ microstructure, as the strengthening contributions of small precipitates were overestimated at the critical transition between weak and strong pair coupling. Jackson and Reed [15] and subsequently Collins and Stone [5] have employed the classic weak and strong pair models to optimise the $\gamma'$ microstructure in Udimet 720Li and RR1000, respectively; their analysis is based upon finding the optimal $\gamma'$ size where the transition between the weak and strong pair coupling occurs and maximum strength can be achieved. Although higher strengths were achieved, it was not possible to fully predict the yield strength, since the analysis was limited to the behaviour of tertiary $\gamma'$ particles with small volume fraction. These results confirm the need to revisit the classic models of weak and strong pair–coupling, identifying the origin of their limitations.

The objective of this work is to postulate a modelling approach to describe the yield stress evolution in superalloys with unimodal and multimodal $\gamma'$ size distributions. This is based upon reviewing classic models on $\gamma'$ shearing and identifying relevant terms not previously considered. The model will then be extended to account for multimodal particle size distributions, where the strengthening contribution of different particle sizes will be weighted according to the relative particle number in the alloy. This allows us to fully describe the factors contributing to the strength of polycrystalline superalloys. Possible scenarios are discussed to improve the yield strength in multimodal superalloys by considering variations in the $\gamma'$ size distributions. The study is mostly focused on alloys produced by powder metallurgy due to their final microstructure being more homogeneous than alloys produced by the cast–and–wrought route [1].

## 2 Modelling precipitate shearing

### 2.1 Classic approaches

Classic precipitation hardening approaches rest on the precept that the bowing angle of a dislocation dictates the critical conditions for cutting point–like particles of small volume fraction (weak pair–coupling) [7, 8]. This concept was later extended to account for the effects of large precipitates where the strong pair–coupling mechanism features [8–11]. These approaches are defined for unimodal size distributions of precipitates. The models are based upon the fact that dislocations pair–up to cut through the $\gamma'$ particles, where a second dislocation glides in the same plane to remove the antiphase boundary introduced by the leading dislocation. Two situations are conventionally distinguished, the weak and strong pair coupling. The main difference between these configurations lies in the length of the bowing dislocations driving particle cutting, as this controls the maximum force a particle of a given size can resist; this length is controlled by the bowing angle $\varphi$ [7]. Figure 1(a) and (b) show schematic illustrations of the weak and strong pair configurations, respectively, where the leading and trailing dislocations are represented by $CB_1$ and $CB_2$, respectively.

The critical resolved shear stress is obtained by evaluating the force balance per particle acting at dislocations $CB_1$ and $CB_2$ [12] and it is given by the contributions of [13]: a) the effective Peach-Koehler force of the applied stress acting on each line segment, b) the repulsive force between the partials; and 3) an opposing force of the antiphase boundary preventing cutting of the $\gamma'$. This can be mathematically expressed as [9]:

$$\begin{aligned} \tau_p b\Lambda_1 + F_{pair}\Lambda_1 - \gamma_{APB} l_1 = 0 \\ \tau_p b\Lambda_2 - F_{pair}\Lambda_2 + \gamma_{APB} l_2 = 0 \end{aligned} \tag{1}$$

where $\tau_p$ is the applied shear stress; $\Lambda_1$ and $\Lambda_2$ are the lengths of the $CB_1$ and $CB_2$ dislocations driving particle cutting, respectively [16]; $F_{pair}$ is the dislocation pair force per unit length; $\gamma_{APB}$ is the antiphase boundary energy; and $l_1$ and $l_2$ are the segment lengths of dislocations $CB_1$ and $CB_2$ cutting the ordered particles, respectively.

In the weak pair case ($\varphi < 180°$) it is considered that the bowing dislocation ($CB_1$) has fully sheared the particles between $CB_1$ and $CB_2$ and $l_1 = 2r$, where $r$ is the mean particle radius. The critical resolved shear stress equals [1]:

$$\tau_p^{Weak} = \frac{\gamma_{APB}}{2b}\left(\left(\frac{6\gamma_{APB}rf}{2\pi T_{ten}}\right)^{1/2} - f\right), \tag{2}$$

$f$ is the particle volume fraction, $T_{ten} = \frac{1}{2}\mu b^2$ is the dislocation line tension, $\mu$ is the shear modulus and $b$ is the magnitude of the Burgers vector. The original model developed by Raynor and Silcok [8] and Brown and Ham [7] included a factor of 1/2 inside the square root, however Reed [1] explored more in detail the force balance in the vicinity of a particle and found that this factor was not necessary. The second term in the equation represents the force produced by the antiphase boundary of the sheared particle (by $CB_1$) in $CB_2$ $\gamma_{APB}l_2/\Lambda_2$ (Third term in equation 1). This equation has been commonly employed in the literature [7–10], although further modifications have also been introduced by other authors [14,17]. For instance, Ardell *et al.* [17] proposed a modified version of the previous force balance, by incorporating size and shape effects from spherical particles affecting the area sheared by dislocations. More recently, Kozar *et al.* [14] have followed a similar approach by considering size effects of particles affecting the mean particle spacing; this assumption appears to be more realistic since the force balance effectively occurs at the dislocation–$\gamma'$ interface, rather than at the centre of a point–like particle. The critical resolved shear stress by these models are as follow:

$$\begin{aligned}
\tau_p^{Ardell} &= \frac{\gamma_{APB}}{b}\left(\frac{-B + \sqrt{\frac{1}{3}B^2 + 4B}}{2\left(1 - \frac{1}{6}B\right)} - f\right) \\
\tau_p^{Kozar} &= \frac{\gamma_{APB}}{b}\left(\sqrt{\frac{\gamma_{APB}r}{T_K}}\frac{r}{L_s} - \frac{\pi}{2}\left(\frac{r}{L_s}\right)^2\right),
\end{aligned} \tag{3}$$

where $B = \frac{3\pi\gamma_{APB}fr}{32T_{ten}}$, $L_s = \left(\frac{8}{3\pi f}\right)^{1/2}2r - 2r$ and $T_K = \frac{\mu b^2}{4\pi}\frac{1-0.25\nu}{1-\nu}\ln\left(\frac{10\text{nm}}{b}\right) = 0.36\mu b^2$, where $T_K$ is a modifed version of the dislocation line tension. It interesting noting that in the case of $\tau_p^{Weak}$ and $\tau_p^{Kozar}$, the shear stress displays a parabolic relationship in $r$ and $f$, whereas in Ardell's model the relationship is more complicated. Figure 2(a) shows the predictions of the room–temperature critical resolved shear stress employing these models

in a NiAl single–crystal alloy as a function of $(r/f/T_{Ten})^{1/2\dagger}$ for $f = 5$ %. The physical parameters for this material are [11]: $\gamma_{APB} = 0.14$ J/m$^2$, $\mu = 80$ GPa, $b = 0.248$ nm. First, it is clearly observed that "negative" strengthening is predicted by the Weak pair and Ardell models, effects which increase as $f$ increases according to $\frac{\gamma_{APB}}{b} f$ (second term in $\tau_p^{Weak}$ and $\tau_p^{Ardell}$, respectively); this discrepancy is due to overestimating the pinning effects in the force balance acting on the trailing dislocations that lead to negative values. Secondly, both the Weak pair and Kozar's models follow a parabolic law, whereas the experimental results show weaker dependence in the $\gamma'$ radius [17]. This could be due to the approximation of point–like obstacles not longer being valid and the presence of additional force terms in equation 1, reducing the resolved shear stress as $r$ increases.

When the $\gamma'$ size is larger than the dislocation pair spacing (strong pair–coupling case), the force balance is modified to account for the leading dislocation being practically straight (no bowing effects as the bowing angle is $\approx 180°$ [7]) and partially cutting the precipitate. In addition, it is considered that the maximum repulsive force of the precipitate occurs when the second dislocation is just in contact with the particle and no repulsive force is present in $CB_2$ (Figure 1(b)). The critical resolved shear stress equals [1, 9]:

$$\tau_p^{Strong} = \frac{\gamma_{APB} l_1}{2bL} = \sqrt{\frac{3}{2}} \left( \frac{\mu b}{\pi^{3/2}} \right) \frac{f^{1/2}}{r} \sqrt{\frac{2\pi\gamma_{APB} r}{\mu b^2} - 1}, \tag{4}$$

where $L$ is the mean particle spacing

$$L = \left( \frac{2\pi}{3f} \right)^{1/2} r, \tag{5}$$

Kozar *et al.* [14] have employed a similar expression but they have introduced an additional factor in the denominator to account for the size of the precipitates: $L - 2r$[‡]. The weak and strong pair models are compared with experiments for wide $\gamma'$ radii ranges and volume fraction to highlight their features and limitations. Figure 2(b) shows the experimental results (dots) at room–temperature for the resolved shear stress variations $\Delta\tau_p$ divided by $\sqrt{f}$ in Nimonic PE16 as a function of the mean $\gamma'$ radius for $f = 8$ %. $\gamma_{APB}$ is 0.14 J/m$^2$ [8], and $\mu = 80$ GPa and $b = 0.248$ nm were considered; the exper-

[†] $(r/f/T_K)^{1/2}$ is adopted for Kozar's model.

[‡] This expression is not considered in this work since it is very close to equation 4.

imental data were obtained from [8, 9]. The predictions by the strong (equation 4) and weak (equation 2) pair coupling are shown by the dashed and dotted lines, respectively. $\Delta\tau_p$ was experimentally determined by removing the stress obtained in as–quenched conditions (before any heat treatment), hence these values do not strictly represent $\tau_p$ since grain boundary strengthening and solid solution hardening might affect the experimental estimates [8]; a constant of 100 MPa/$f^{1/2}$ was added to the models account for other possible strengthening effects; this constant was fixed for all particle sizes. The strong pair model displays apparent agreement with the measurements, and the transition between weak and strong coupling seems accurate, although $\tau_p^{Weak}$ has negative stress values (up to $-(\frac{\gamma_{APB}}{b}f)/f^{1/2}$=-80 MPa/$f^{1/2}$) for small $r$ and the "offset" stress described above is needed. However, considerable discrepancies arise for high $\gamma'$ volume fraction; Figure 2(c) shows the experimental observations (dots) on the effect of the $\gamma'$ size to the room–temperature resolved shear stress (divided by $\sqrt{f}$) in Nimonic 105 and the predictions by the weak (dotted line) and strong (dashed line) pair coupling models when $f$ = 55 % and $\gamma_{APB}$ = 0.11 J/m$^2$ [9]; experiments were obtained from [9]. Again in this case an offset value of 175 MPa/$f^{1/2}$ is added to the models to match the experimental data. It is observed that the strong pair model diverges from the experimental measurements for $\gamma'$ with radius below $\sim$ 90 nm predicting stress discrepancies up to 100 MPa and the weak pair model underpredicts most of the experiments. Moreover, the weak pair model predicts "negative" strengths of up to $-(\gamma_{APB}/bf)/f^{1/2}$ =-163 MPa/$f^{1/2}$ for $\gamma'$ radii up to $\sim$ 7nm (this it is not directly observed in Fig. 2(b), since the 175 MPa/$f^{1/2}$ offset stress is higher than the predicted negative stress). Possible explanations of the discrepancies in the strong pair model can be related to the modifications in the effective length of the dislocation passing through the precipitates; it was arbitrarily considered that the leading dislocation is straight for all particle sizes ($\varphi = 180°$), although it has been pointed out by other authors [12, 13] that the leading dislocation might still bow out and not fully shear the particle ($\varphi < 180°$). These results also confirm that the weak pair coupling model is not valid for high $\gamma'$ volume fraction.

Additionally, the most critical limitation of these models is that none of them address

specifically the critical range where maximum strength occurs, as they are formulated to consider extreme dislocation configurations and assume them to converge at the transition from the weak and strong pair coupling; however, since the models are incompatible, there is no smooth transition in the driving force for particle cutting when dislocation bow–out occurs (weak pair, Figure 1(a)) and when the leading dislocation is straight (strong pair, Figure 1(b)). This leads to inconsistent predictions in the transition regime that only seem apparent at low $\gamma'$ volume fractions. The discrepancies are crucial when considering multimodal superalloys, since the tertiary $\gamma'$ lies in the range of disagreement of these models, and the volume fraction of $\gamma'$ is 40–60 %. The next section will introduce the respective modifications to these models in order to obtain a unified description of $\tau_p$ in unimodal and multimodal $\gamma'$.

### 2.2 Unified approach

The limitations of the weak and strong pair models are summarised as follows:

(i) No detailed analysis at the transition between weak and strong pair coupling configurations has been properly introduced.

(ii) A "negative" strengthening effect is predicted by the weak pair model for particles with small radius.

(iii) The equilibrium force balance in the strong pair–coupling case has been defined between dislocations and point–like particles, which remains valid for low volume fractions.

(iv) Higher stress levels were predicted by the strong pair–coupling model in alloys with high precipitate volume fraction and radii close to the transition between the weak and strong pair configurations.

(v) A "stiff" particle size dependence on the weak pair model is observed for larger particles.

Although it has traditionally been assumed that the maximum particle strength occurs when the weak and strong pair–coupling models converge [1, 13], by definition, these

models rest on the basis that the maximum particle strength occurs when the bowing angle of the leading dislocation ($\varphi$, Fig. 1(a)) is practically null [7,8]; Brown and Ham [7] have pointed out that this occurs when $T_{ten} \approx \gamma_{APB} r$, as $\varphi = 2\text{acos}\left(\frac{\gamma_{APB} r}{T_{ten}}\right)$ [7]. In addition, Nembach *et al.* [18] have also pointed out that the maximum particle force occurs when the leading dislocation crosses the diameter of the particle, and the transition between weak and strong pair occurs when the particle size is such that the cutting force by the leading dislocation is no longer able to fully penetrate half of the particle[§]; this occurs when the dislocation line tension equals half the repelling force of the particle [11, 16]: $\gamma_{APB} r = \frac{1}{2}\mu b^2$; this relationship fulfils the null–bowing angle condition [7]. Thus, the particle radius with maximum strength is equal to:

$$r_m = \frac{\mu b^2}{2\gamma_{APB}}. \tag{6}$$

The weak and strong pair–coupling configurations are then dictated when $r < r_m$ and $r > r_m$, respectively. The negative stress in the weak pair model (item ii)) originates from the repulsive force of a particle pinning the second dislocation (Figure 1(a)); details on the force balance derivation for this case can be found in [1]. This force term is introduced under the assumption that the leading dislocation has already sheared a number of particles and dislocation $CB_2$ is present to restore internal order in the precipitates. Although this configuration has been widely observed in experiments, this arrangement represents stress levels above the critical resolved shear stress ($\tau > \tau_p^{Weak}$), since the first dislocation has already sheared the particles between $CB_1$ and $CB_2$ and glide already occurred, *i.e.* dislocations have already induced substantial plastic strain. This implies that the dislocation configuration displayed in Figure 1(a) does not represent the dislocation configurations at the critical resolved shear stress (*i.e.* before inducing plastic strain) but rather at higher stress levels. A modified configuration for $\tau_p$ is represented by the leading dislocation just shearing the first particle, whilst the trailing dislocation is just about to enter the second particle to restore internal order. Figure 3(a) shows a schematic representation of the modified configuration, in which dislocation $CB_1$ has only sheared

[§]The ordering force is maximum at the particle's diameter, hence the force on the second half of the particle is lower and it will be easily sheared once the dislocation has reached its diameter.

one line of particles at the resolved shear stress. This implies that no pinning force from the antiphase boundary is present in $CB_2$ and $\gamma_{APB} l_2 = 0$ in equation 1.

For the case of the strong pair–coupling, the length of $CB_1$ cutting the precipitates, $l_1$, is derived by obtaining the distance to which a particle is penetrated, measured from the point of entry [1]. Figure 3(d) shows a schematic representation of the geometric configuration between $l_1$ and $r_m$ for a particle with mean radius $r$[¶]. Following the procedure outlined in [1], this implies that $l_1$ is given by $l_1 = 2(r^2 - (r - r_m)^2)^{1/2}$ for $r \geq r_m$. Hence the length of the leading dislocation cutting the precipitates can be expressed as:

$$l_1 = \begin{cases} 2r & \text{if } r < r_m \text{ (Weak pair–coupling)} \\ 2\big(r^2 - (r - r_m)^2\big)^{1/2} & \text{if } r \geq r_m \text{ (Strong pair–coupling).} \end{cases} \tag{7}$$

This result unifies the effective extent of particle shearing in the force balance (equation 1), whilst providing smooth transition between both configurations. To remove the point–like defects assumption in the strong pair model (item iii)), a correction term on the effective distance between obstacles being sampled by a dislocation has been previously employed by several authors [13, 14, 17]. This consists of subtracting the length of the dislocation cutting the ordered particle ($l_1$) from the mean particle spacing $L$, defining an effective particle spacing ($L - l_1$), as this segment length no longer features in the shear process [11, 13], as schematically shown in Figure 3(c).

Higher stress levels by the strong pair–coupling close to the transition regime (item iv)) results from arbitrarily replacing the length of $CB_1$ acting as driving force for cutting the precipitate $\Lambda_1$: In the case of the weak–pair coupling, the Friedel sampling length $\lambda_1$ is used for $\Lambda_1$, as it represents the mean distance between obstacles being sampled by a bowing dislocation along its length [16]:

$$\lambda_1 = \left(\frac{T_{ten}}{\gamma_{APB} r}\right)^{1/2} L, \tag{8}$$

where the ratio $(T_{ten}/\gamma_{APB} r)^{-1}$ is linked to the bowing angle required for cutting particles [16]. In the strong pair model, it is assumed that the leading dislocation is practically straight (the bowing angle is close to 180 °), since the precipitate size is large. Hence

[¶]In Hüther and Reppich original approach, the dislocation pair/particle configuration was simplified by considering the particles homogeneously distributed, hence $r$ is employed.

$\Lambda_i$ is considered equal to the effective particle spacing $(L - l_1)$. However, it has been pointed out by Nembach [12] that an intermediate configuration can exist (medium pair–coupling), where the dislocation pair partially cuts the particle (strong case), but $CB_1$ will bow out to increase the applied force (weak case); this configuration was observed in Nimonic 105 with $\gamma'$ radius of 37.5 nm [10], but was ignored to simplify the model. Figure 3(c) shows a schematic representation of this configuration. This implies that the Friedel spacing should also feature in the strong pair regime, at least for smaller particles, whilst $L - l_1$ is appropriate for larger $\gamma'$ when $\varphi \approx 180°$. Thus, a unified distance $\Lambda_1$ between the obstacles being sampled by a bowing/straight leading dislocation can be defined as:

$$\Lambda_1 = \max(\lambda_1, L - l_1) = \max\left(\left(\frac{T_{ten}}{\gamma_{APB} r}\right)^{1/2} L, L - l_1\right). \tag{9}$$

This equation is well defined since the ratio $T_{ten}/\gamma_{APB} r > 1$ for small $r$ and it decreases eventually reaching $L - l_1$, where a smooth transition occurs between these parameters. To illustrate how the omission of the intermediate configuration affects the strong pair model, Figure 4 shows the Friedel spacing $\lambda_1$ and the effective mean particle spacing $L - l_1$ variations with $r$ and the respective variations in $\Delta\tau_p/\sqrt{f}$ in Nimonic 105 using the same parameters as in the previous section; the transition between weak and strong pair coupling occurs at $r_m = 22$ nm. It is observed that the classic strong pair–coupling model diverges from the experiments in the range where $\lambda_1 \sim L - l_1$ (70–100 nm), suggesting that $\Lambda_1$ is more appropriate for describing the driving force acting on the leading dislocation, as $\tau_p$ is inversely proportional to $\Lambda_1$ [9] and $\lambda_1$ is higher than $L - l_1$ for $r < 125$ nm.

With respect to deviations from the weak pair model (item v)), we consider the effects of the applied stress acting on spherical particles in the force balance. Although the cutting stress for the $\gamma'$ is high ($\gamma_{APB}/b \sim 560$ MPa for $\gamma_{APB} = 0.14$ J/m$^2$), the force of the applied stress acting on the particle becomes higher as the $\gamma'$ size increases, $2\tau_p br$. This term affects the critical stress for dislocation cutting as the "effective" strength of the particle decreases when increasing the $\gamma'$ size and better matching the experimental results shown Fig. 2(a).

These modifications remove the limitations of the classic weak and strong pair approaches and the force balance in equation 1 is now given by:

$$\tau_p b\Lambda_1 + F_{pair}\Lambda_1 - \gamma_{APB} l_1 + 2\tau_p br = 0$$
$$\tau_p b\Lambda_2 - F_{pair}\Lambda_2 = 0. \tag{10}$$

It is worth noting that it is not necessary to estimate $\Lambda_2$ and $F_{pair}$, since these terms cancel out when simplifying both expressions. Finally, by rearranging these equations, the unified critical resolved shear stress $\tau_p$ for all particle sizes equals:

$$\tau_p = \frac{\gamma_{APB} l_1}{2b(\Lambda_1 + 2r)}, \tag{11}$$

where $l_1$ and $\Lambda_1$ are given in equations 7 and 9, respectively. This equation successfully captures the gradual transition from the weak and strong pair coupling configurations, via the transition in the values of $\Lambda_1$ and $l_1$. Figure 5 shows the model predictions (solid lines) employing this equation in (a) NiAl, (b) Nimonic PE16 and (c) Nimonic 105 employing the same parameters than in Figure 2[‖]; in (a) a $\gamma'$ volume fraction of 34 % was considered to show wider $\gamma'$ size range in the results. More accurate predictions are observed in almost all cases when compared to the experimental data. Moreover, the limitations of the previous models have been successfully removed: in Fig. 5(a) the weak pair–coupling regime is accurately described for different $\gamma'$ sizes and no negative stress values are predicted; these results also illustrate that the force term of the applied stress acting on the particle ($2\tau_p br$) is responsible for removing the "stiffness" in the weak pair–coupling model (via the $2r$ term in the denominator in equation 11) and that the modified dislocation configuration is accurate (Figure 3(a)). Although in (b) the model applied to Nimonic PE16 predicts the maximum stress to be at $2r \approx 35$ nm whilst the experiments show an apparent peak at $2r \sim 25$ nm for low $\gamma'$ volume fraction, it does accurately describe the peak stress in (c) when increasing $f$ to 55 % in Nimonic 105. The discrepancy in (b) can be attributed to considering low values for $\gamma_{APB}$, since higher energy values have been employed by other authors [18]. In Fig 5(c), one can note that

[‖]In the case of Nimonic 105, the "offset" stress is set 200 MPa $/f^{1/2}$ since the finite particle size effects $(L - l_1)$ predict slightly lower stress values.

the model accurately describes both the small and large $\gamma'$ regimes, and this is attributed to the introduction of the parameter $\Lambda_1$, providing a smooth transition as opposed to the weak and strong pair models that extrapolate from incompatible configurations (Fig. 2(c)). These results corroborate the complete description for all precipitate sizes with high volume fraction. Modifications to account for multimodal size effects can now be introduced, although the Orowan stress for large particle size needs to be introduced first.

### 2.3 Orowan stress

For sufficiently large precipitates, the stress required for the dislocations to bypass the $\gamma'$ is lower than the stress required for the dislocations to cut the particles and the Orowan bypassing mechanism operates [13]. The Orowan shear stress is given by [13]:

$$\tau_{Oro} = \frac{3\mu b}{2L}. \tag{12}$$

$\tau_{Oro}$ is valid for $\gamma'$ sizes when the stress required for the dislocations to bypass the $\gamma'$ is lower than the stress required for the dislocations to cut the particles; the critical radius $r_{Oro}$ for transition occurs when $\tau_p = \tau_{Oro}$.

## 3 Multimodal precipitate distribution effects

The main challenge in extending the previous models for alloys with unimodal and multimodal size distributions is to estimate the respective contribution to the critical resolved shear stress $\tau_p$ of each particle. RR1000 containing unimodal $\gamma'$ has shown higher yield stress than that for a microstructure containing secondary and tertiary precipitates at room temperature [5]. This indicates that during uniaxial tensile deformation a constant strain rate constraints dislocations to shear the particles simultaneously in order to accommodate the imposed strain levels.

The force balance in equation 10 is defined for individual dislocation/precipitate events. This assumes that the force balance applies to each particle according to its different size. The particle shear stress and Orowan bowing in superalloys with multimodal $\gamma'$ size are then the sum of the individual dislocation/particle interaction events, where the relative strength of the particles is given by the $\gamma'$ size distribution $p$. The

total volume fraction ($f$) and particle size distributions are captured by the total particle number density [19]. If $p$ is fitted to a continuum function, this is expressed as:

$$\begin{aligned} \tau_p &= \int_0^{r_{Oro}} \frac{\gamma_{APB} l_1}{2b(\Lambda_1 + 2r)} p dr \\ \tau_{Oro} &= \int_{r_{Oro}}^{\infty} \frac{3\mu b}{2L} p dr. \end{aligned} \tag{13}$$

If a typical superalloy contains primary, secondary and tertiary $\gamma'$, the particle size distribution can be approximated by a mixed probability function [20]:

$$p = w_p p_p + w_s p_s + w_t p_t, \tag{14}$$

where $w_p$, $w_s$ and $w_t$ is the normalised particle number of primary, secondary and tertiary $\gamma'$, respectively, $(w_p + w_s + w_t = 1)$ and $p_p$, $p_s$, and $p_t$ are the individual size distribution functions of primary, secondary and tertiary $\gamma'$, respectively. $w_i$ is given by the relation: $w_i = N_i/N$, where $N = N_p + N_s + N_t$, and $N_p$, $N_s$, $N_t$ are the particle number of the primary/secondary/tertiary $\gamma'$ in the specimen. $p_i$ are approximated by lognormal distributions since they have shown good correlation with experimental data [5]; additionally, $N_i$ can be obtained if the volume fraction of each $\gamma'$ type $f_i$ is known [1]. $p_i$ and $N_i$ are mathematically expressed as:

$$\begin{aligned} p_i &= \text{Lognorm}(r_i, \omega_i) = \frac{1}{\sqrt{2\pi} r} \exp\left( - \frac{\left(\ln(r) - \ln(r_i) + \omega_i^2/2\right)^2}{2\omega_i^2} \right), \\ N_i &= \frac{f_i}{\pi \int_0^{\infty} r^2 p_i dr} = \frac{f_i}{\pi r_i^2 \exp(\omega_i^2)}, \end{aligned} \tag{15}$$

where $r_i$ is the mean particle radius and $\omega_i$ is a constant related to $r_i$ and the standard deviation $s_i$ of the size distribution [5]: $\omega_i^2 = \ln\left(1 + \left(\frac{s_i}{r_i}\right)^2\right)$. The denominator in $N_i$ accounts for the total area in the specimen, since most of the experimental characterisation has been performed from two dimensional micrographs; hence $f_i$ effectively describes an area fraction. Combining equations 13, 14 and 15, the precipitation contribution to the yield stress is given by:

$$\begin{aligned}\tau_p &= \int_0^{r_{Oro}} \frac{\gamma_{APB} l_1}{2b(\Lambda_1 + 2r)}(w_p p_p + w_s p_s + w_t p_t)dr, \\ \tau_{Oro} &= \int_{r_{Oro}}^{\infty} \frac{3\mu b}{2L}(w_p p_p + w_s p_s + w_t p_t)dr. \end{aligned} \tag{16}$$

The total fraction $f = f_p + f_s + f_t$ is employed to estimate $\Lambda_1$; this is to represent the effective mean particle spacing [19]. It is interesting to note that one can isolate the individual contributions to the particle shear stress of the secondary and tertiary $\gamma'$ size by considering $\int_0^{r_{Oro}} \tau_p w_s p_s dr$ and $\int_0^{r_{Oro}} \tau_p w_t p_t dr$, respectively, as $w_i p_i$ provides the weighted contribution of the respective size range. Moreover, the weak and strong pair–coupling relative contributions can also be obtained: $\tau_p = \tau_p^{Weak} + \tau_p^{Strong} = \int_0^{r_m} \tau_p p dr + \int_{r_m}^{r_{Oro}} \tau_p p dr$.

It is interesting noting that although a rigorous analysis on the $\gamma$' distribution is considered in this work, it is possible to estimate precipitation contribution by using only the average values of the distinct $\gamma'$ particles ($r_p$, $r_s$ and $r_t$). This can be done if the following individual size distributions are considered in equation 15: $p_i = \delta(r - r_i)$, where $\delta(r)$ is the Dirac delta function. By the properties of the Dirac delta function, the integrals in equations 15 and 16 are simplified**. This result gives: $N_i = \frac{f_i}{\pi \int_0^{\infty} r^2 p_i dr} = \frac{f_i}{\pi r_i^2}$, and the number fraction is $w_i = \frac{f_i}{r_i^2} / \left( \frac{f_p}{r_p^2} + \frac{f_s}{r_s^2} + \frac{f_t}{r_t^2} \right)$. If it is assumed that $r_s < r_{Oro}$ and $r_p > r_{Oro}$ [14], $\tau_p$ and $\tau_{Oro}$ are simplified to:

$$\begin{aligned}\tau_p &= \int_0^{r_{Oro}} \frac{\gamma_{APB} l_1}{2b(\Lambda_1 + 2r)}(w_p p_p + w_s p_s + w_t p_t)dr \\ &= \frac{\gamma_{APB}}{2b}\left( w_s \frac{l_1^s}{(\Lambda_1^s + 2r_s)} + w_t \frac{l_1^t}{(\Lambda_1^t + 2r_t)} \right), \\ \tau_{Oro} &= \int_{r_{Oro}}^{\infty} \frac{3\mu b}{2L}(w_p p_p + w_s p_s + w_t p_t)dr \\ &= w_p \frac{3\mu b}{2L^p}, \end{aligned} \tag{17}$$

where $l_1^i$ and $\Lambda_1^i$ are calculated using equations 7 and 9, respectively, and $f = f_p + f_s + f_t$ is employed in all cases. This equation confirms that the overall strengthening contribution of primary, secondary and tertiary $\gamma'$ is not only determined by the additions of their respective critical resolved shear stress but it is also controlled by their relative

** $\int_{\infty}^{-\infty} f(r)\delta(r - r_0)dr = f(r_0)$.

number fraction (via $w_i$). Previous approaches describing precipitation strengthening in multimodal $\gamma'$ had ignored the latter [14]. Comparison between the values of equations 16 and 17 are shown in Section 7.

## 4 Yield stress

The yield stress $\sigma_Y$ in superalloys includes four strengthening contributions [21]: *i*) Grain boundary ($\sigma_D$); *ii*) solid solution in $\gamma$ ($\sigma_{ss}$); *iii*) precipitation shearing ($\sigma_p = M\tau_p$), where $M$ is the Taylor orientation factor and it is equal to 3 [22]; and *iv*) Orowan bypassing ($\sigma_{Oro} = M\tau_p$) [13]:

$$\sigma_Y = \sigma_D + \sigma_{ss} + \sigma_p + \sigma_{Oro}. \tag{18}$$

$\sigma_D$ is represented by the Hall–Petch relationship [13]: $\sigma_D = \frac{k_Y}{\sqrt{D}}$, where $D$ is the mean grain size and $k_Y$ is the Hall–Petch constant which value in superalloys has been experimentally estimated to lie in the range 710–750 MPa $\mu$m$^{1/2}$ [6, 14]; 710 MPa $\mu$m$^{1/2}$ is used in our calculations.

Solid solution hardening is estimated by employing Labusch [23] theory: The increment in the yield stress results from solute atoms acting as frictional obstacles for dislocation slip in a binary alloy [23]. Such is controlled by the local lattice and modulus change in around in the solid solution. Gypen and Deruytterre [24,25] later extended this approach to integrate the strength increments by various alloying elements in multicomponent systems. This gives $\sigma_{ss}$ to be equal to: $\sigma_{ss} = (1-f)\big(\sum \beta_i^{3/2} x_i\big)^{2/3}$, where the $(1-f)$ factor is to account for solid solution contribution confined to the $\gamma$, as dislocation slip mostly occurs at the matrix; $x_i$ is the atom fraction of substitutional element $i$ in the $\gamma$; and $\beta_i$ are constants related to the lattice and modulus misfit of element $i$ with Ni in the binary system. The value of $\beta_i$ has been derived by Fleischer [26] and it equals: $\beta_i = \frac{3}{2}\mu(\eta_i' + 16\delta_i)^{3/2}$, where $\eta_i' = |\eta_i|/(\eta_i + 0.5)$ is a constant; $\eta_i = \frac{\mu_i - \mu_{Ni}}{\mu_{Ni}}$ and $\delta_i = \frac{r_i^a - r_{Ni}^a}{r_{Ni}^a}$ are the modulus and lattice strain of element $i$ with respect to Ni, respectively; and $\mu_i$ and $r_i^a$ are the shear modulus and atomic radius of element $i$, respectively. Estimation of $\beta_i$ is shown in the Appendix.

## 5 Results

The model results of the yield stress are tested against experimental measurements in five additional superalloys containing unimodal and multimodal $\gamma'$ size distributions. Table 1 shows the chemical composition of the commercial alloys referred to in this work as well as the total $\gamma'$ volume fraction ($f$), covering a wide compositional range and volume fraction; $f$ values were obtained from the literature. No carbides, interstitial elements or substitutional elements with concentrations less than 1 wt% are considered in this work, since their strengthening contribution is relatively low in superalloys [1]. For $\sigma_{ss}$, the chemical composition in the $\gamma$ for the alloys tested is displayed in the Appendix.

Table 2 shows the initial microstructures for these alloys obtained with different heat treatments. The experimental measurements were obtained from the literature. In the case of alloys with unimodal $\gamma'$ size distributions the volume fraction and mean size are displayed in $f_s$ and $r_s$, respectively. For the case of RR1000, the measured values of the grain size and $\gamma'$ ($f_i$ and $r_i$) reported in [6] are added as supplementary material. This also includes the parameters $\omega_i$ obtained in the lognormal size distributions, as well as the particle size distributions of secondary $\gamma'$. Requests for access to additional experimental data should be directed to the corresponding author and will be considered against commercial interests and data protection.

$\sigma_Y$ is obtained by solving equations 16 and 18. The first step for each simulation is to identify the $\gamma'$ size distribution and to numerically solve the integrals in equations 15 numerically. $p_i$ is obtained by inserting the mean radius for each size range (primary, secondary and tertiary) given in Table 2 into equation 15; $\omega_i$ values in equation 15 were estimated from the experimental standard distributions and in the case where no information were provided, these parameters are approximated to typical experimental values [5, 6]: $\omega_p = 0.05$, $\omega_s = 0.25$ and $\omega_t = 0.25$. For the numeric integration, a particle size interval was taken equal to $dr \approx \Delta r = 0.1$ nm and the maximum $\gamma'$ radius in the integral was fixed to 10,000 nm (the maximum mean primary $\gamma'$ radius is 1000 nm). This spans a very wide particle size distribution in the range $0.1 \leq r \leq 10,000$ nm. The values of the antiphase boundary energy were assumed identical in all alloys tested, except for Udimet 720Li.

$\gamma_{APB}$ values were obtained from theoretical predictions in RR1000 employing the CALPHAD method [5]; these values were fitted to a polynomial function to capture the temperature effects: $\gamma_{APB} = (0.28 - 7\times10^{-6}T - 3\times10^{-8}T^2)$ J/m$^2$; this expression is consistent with observations on the temperature dependence of the antiphase boundary energy [27]. In the case of Udimet 720Li, it has been pointed out that $\gamma_{APB}$ is slightly higher [15]; hence, its value is increased by 0.02 J/m$^2$: $\gamma_{APB} = (0.3 - 0.000007T - 0.00000003T^2)$ J/m$^2$. Although the shear modulus employed in the model should be that for the matrix, as dislocation generation and glide occur mostly in the $\gamma$, in practice it is difficult to measure the elastic constants of the phases in isolation on each alloy [28]; hence, $\mu$ is taken as the modulus of the alloy to simplify the analysis. $\mu$ in RR1000 is obtained from the Young modulus' measurements in [29], with $\mu = \frac{E}{2(1+\nu)}$ and $\nu = 0.32$. These values were fitted to analytical expressions to capture their temperature variations (in K) and simplify calculations: $\mu = 87.32 - 0.0009T - 0.000019T^2$ GPa; this expression was assumed valid for other alloys tested as the variations of $\mu$ with composition are small [1]. $b = 0.248$ nm was used for all alloys tested.

Figure 6(a) shows the yield stress predictions in ATI 718Plus at room temperature (black line) and KM4 (purple line) at 650 °C with unimodal $\gamma'$ distributions and the experimental measurements for these alloys; the horizontal axis represents the mean particle radius. In this this case, $w_s = 0.25$[††] and $f_p = f_t = 0$. The model shows generally good agreement with experiments for large $\gamma'$ (strong pair–coupling regime) in KM4 and for smaller $\gamma'$ (weak and medium pair–coupling) for ATI 718Plus; the model successfully predicts the maximum strength in ATI 718Plus to take place at $r \sim 15$nm. It is interesting to note that He *et al.* [30] observed the maximum yield stress in Inconel 718 also occurred at $r \approx 15$ nm. Additionally, predictions for ATI 718Plus employing the classic weak and strong pair–coupling models (including solid solution and Hall–Petch strengthening) in equations 2 and 4 are shown; the combined weak–strong models predict higher stress levels of up to $\sim 120$ MPa with respect to the experimental measurements in the vicinity of the maximum stress. This further confirms that our model is able to successfully

[††]The values of $\tau_p$ for unimodal $\gamma'$ are practically the same as if one simply employs equation 11, as the size distribution functions are very narrow.

capture the transition between the weak and strong pair configurations and illustrates the limitations of the previous models. Figure 6(b) shows the yield stress predictions in KM4 holding multimodal $\gamma'$ size distributions (subsolvus and supersolvus conditions) and in Udimet 720Li following different heat treatments and at different temperatures up to 650 °C [15, 31]. Figure 6(c) and (d) show the simulated $\gamma'$ size distributions in KM4 (only mean values were reported in the experiments) and Udimet 720 Li (HT1–3), respectively, and $r_m$ values; experimental distributions for 720Li are also shown in (d). The model shows good agreement with the experimental trends, however discrepancies in 720Li of up to 150 MPa are shown for HT1 and HT3 and up to 50 MPa for the results obtained from Gopinath *et al.*; for the case of KM4 Subsolvus, the model underpredicts $\sigma_Y$ by 70 MPa. The discrepancies in HT1 and HT3 could be due to the size distribution characterisation, as the number density of tertiary $\gamma'$ displayed in the original micrograph appears to be much higher than the values reported in Figures 6(d) [15]. The additional discrepancies can be due to the parameters in the particle size distribution differ from those corresponding to each alloy. These results show that our model is able to describe the yield stress in the same alloy (KM4) when it holds unimodal (a) and multimodal $\gamma'$ (b). Furthermore, to illustrate the differences in $\sigma_Y$ between subsolvus and supersolvus heat treatments, in KM4 the strengthening contributions for subsolvus heat–treatment conditions are $\sigma_D$ = 290 MPa, $\sigma_{ss}$ =92 MPa , $\sigma_p$ =590 MPa ($\sigma_p^{weak}$ = 0.01 MPa and $\sigma_p^{strong}$=590 MPa) and $\sigma_{Oro}$ =40 MPa, whereas in supersolvus the strengthening contributions are $\sigma_D$ = 95 MPa, $\sigma_{ss}$ = 80 MPa, $\sigma_p$ =739 MPa ($\sigma_p^{weak}$ =17 MPa and $\sigma_p^{strong}$=722 MPa) and $\sigma_{Oro}$ = 7 MPa. By comparing individual contributions, $\gamma'$ strengthening increases (149 MPa) during supersolvus heat treatment although strength loss occurs from grain coarsening (-195 MPa), providing a net strength loss with respect to subsolvus conditions. This result illustrates that grain growth should be avoided in order to maintain high strength and hence the minimum necessary primary $\gamma'$ should be included in the final microstructure.

Figure 7 shows the yield stress predictions at 650 °C and their comparison against the experimental measurements in RR1000 when applying a dual microstructure heat

treatment (DMHT) process on a turbine disk [6,32]; this process induces a temperature gradient between the bore and the rim of the disk and a range of microstructures can be tailored when the disk is heat treated near the $\gamma'$ solvus temperatures; this includes wide range in the grain size and $\gamma'$ volume fraction, which is appropriate for our investigation. A detailed explanation of the heat treatment and a complete microstructure characterisation can be found in [6,32]. Microstructures and yield strengths were measured as a function of the radial distance (in mm) from the bore to the rim. Figure 7(a) shows the yield stress measurements and the model predictions for these very different microstructures. Figure 7(c) and (d) show the measured volume fraction of the $\gamma'$ (including primary, secondary and tertiary) and the mean $\gamma'$ radii and grain size, respectively. It is worth noting that in the "intermediate" region (70–80 mm to the Rim) up to four distinct $\gamma'$ size distributions were observed as the secondary $\gamma'$ displayed a bimodal distribution (see supplementary material); this microstructure was included in the model by adding an extra term in the size distribution to account for the residual secondary $\gamma'$; $\omega_p = [0.04, 0.1]$, $\omega_s = [0.18, 0.35]$ $\omega_t = [0.2, 0.36]$ were directly obtained from the particle size distributions and standard deviations measured in [6]. The model shows very good agreement with the experiments, as discrepancies are lower than 70 MPa and consistent with scatter in the measured volume fractions. Figure 7(b) shows the individual contributions to the total yield stress for these microstructures. $\gamma'$ shear is by far the highest component of strength (540-620 MPa) and increases with $\gamma'$ volume fraction; grain boundary strengthening is the second highest contributor (100-300 MPa) if the grain size is lower than 20 $\mu$m, indicating that a minimum volume fraction of primary $\gamma'$ should be present in order to prevent grain growth (Fig. 7(c)); the lowest contribution is given by the Orowan mechanism as most of the secondary $\gamma'$ is in the region of the strong pair–coupling and primary $\gamma'$ particles are too large. The Results in Figures 6 and 7 confirm that the model is sensitive to variations in the microstructure and it is able to predict the yield stress for wide conditions of multimodal $\gamma'$ sizes.

Figure 8 shows predictions of the yield strength $\sigma_Y$ for two alloys (a) RR1000 and (b) IN100 at different temperatures, compared with experimental measurements; two

microstructures were explored in each alloy (Table 2). In Fig. 6(a) no characterisation on the microstructure was provided; hence, these microstructures were assumed to be equivalent to those in Fig. 6 at 14 and 119 mm to the Rim for coarse and fine grain, respectively, as they are similar to those obtained from the standard heat treatments [6, 32]. The temperature effects on $\sigma_Y$ are assumed to be dominated by $\gamma_{APB}$ and $\mu$ in this temperature range, although temperature variations of the other strengthening mechanisms can be present [1]. The model predictions show very good agreement with the experimental trends in both alloys, except for supersolvus IN100 at 650 °C where the experiments display apparent hardening, whereas the model predicts lower yield stress. This may be due to the assumptions made about the microstructures in this case, since the model predicts the yield strength successfully for both heat treatments of RR1000 where the microstructures were characterised. To assess the relative strength loss between the subsolvus and supersolvus heat treatments in IN100 at 650 °C the respective strengthening contributions for subsolvus conditions are $\sigma_D = 355$ MPa, $\sigma_{ss} = 101$ MPa, $\sigma_p$ =607 MPa ($\sigma_p^{weak}$ =600 MPa and $\sigma_p^{strong}$=7 MPa) and $\sigma_{Oro} = 0.6$ MPa, whereas in supersolvus $\sigma_D = 121$ MPa, $\sigma_{ss} = 101$ MPa, $\sigma_p$ =668 MPa ($\sigma_p^{weak}$ =654 MPa and $\sigma_p^{strong}$=13 MPa) and $\sigma_{Oro} = 0.8$ MPa; a net stress decrease of -173 MPa is associated with supersolvus conditions, similar to the case of KM4 and RR1000. In order to compare how the yield stress differs from unimodal and complex multimodal $\gamma'$ size distributions, Figure 8(c) shows the yield stress predictions in RR1000 and one experimental result [5] as a function of the secondary $\gamma'$ radius with $D = 7$ $\mu$m and $f_p = 7.5\%$ and $r_p = 225$ nm for three different volume fractions ($f = f_p + f_s$). It is worth noting that although this is a bimodal microstructure, the effect of primary $\gamma'$ on $\tau_p$ is very low and it can be considered as unimodal. Based on the classic weak and strong pair models, Collins and Stone concluded that the maximum strength is achieved when $r_s = 30$ nm, however, with our model maximum yield stress is predicted when $r_s = 12-15$ nm; our predictions are in agreement with the observations of He *et al.* [30] in Inconel 718 and in ATI 718Plus (Figure 5(a)). Although the model shows lower values than the experiment by $\sim 50$ MPa, it is predicted that the yield stress is higher by up to 100 MPa for unimodal $\gamma'$ compared with multimodal

size distributions (Figure 6(a), at distance to the Rim$\geq$ 100 mm). This demonstrates that $\sigma_Y$ is higher for unimodal $\gamma'$ than for an alloy containing both secondary and tertiary $\gamma'$. Additionally, marginal increments in strength are observed when increasing the $\gamma'$ volume fraction. To illustrate this, Figure 8(d) shows the model predictions at 650 °C for RR1000 with an unimodal particle size with fine (solid line) and coarse (dashed line) microstructures for different $\gamma'$ volume fractions; $\sigma_Y$ values in a number of common turbine disk alloys with different volume fractions are displayed [1]; the model predictions are within the range of the actual values of these alloys. It is interesting to note that the yield stress nearly saturates for $f > 50\%$, indicating that only marginal increments are expected when increasing the $\gamma'$ volume fraction beyond this point, as it is predicted in (c).

## 7 Discussion

A new model for the yield stress in superalloys with unimodal and multimodal $\gamma'$ size distributions has been presented. It was shown to be valid for very wide range of particle size and $\gamma'$ volume fraction. The model addresses the limitations identified in the classic weak and strong pair–coupling models and introduces more appropriate configurations. These included: 1) the dislocation configuration for the weak pair–coupling case was redefined since the established model represents stress levels higher than the critical resolved shear stress where slip has already occurred; 2) the maximum strength and transition occurs when the dislocation bowing angle is null [7], as opposed to the previous approach where the transition occurs when the (incompatible) weak and strong pair models converge; 3) an intermediate (medium pair–coupling) configuration was identified where dislocations bow out and partially cut the precipitates, allowing us to connect the weak and strong pair coupling configurations; and 4) an additional term in the equilibrium force balance was introduced to account for the force acting from the applied stress on the $\gamma'$. This allowed us to obtain a continuous transition between weak and strong pair–coupling and good correlation was obtained with the experiments; classic approaches do not address in detail the critical range where the transition occurs and rely on the convergence of the

(inconsistent) weak and strong pair models. Moreover, the ability to fully describe the strength of $\gamma'$ with different sizes also allowed us to extend the model when multimodal particle size distributions were present. This was done by weighting the individual contribution to the total strength according to the relative particle number in the alloy. These results were combined with grain boundary and solid solution strengthening models to predict the yield stress in five, and the particle shear strength in three superalloys containing wide variations in microstructure, composition and at temperatures up to 700 °C. Thus, for the first time a parameter–free physics–based model has been able to predict the yield stress in PM superalloys with complex $\gamma'$ microstructures for grain sizes up to 50 $\mu$m.

A rigorous analysis was performed on the effect of multimodal size distributions in precipitation hardening (equation 16). Although this result allows us to consider more complex distributions, it was also shown that particle strengthening can be approximated if only the mean radii of each particle type are considered (equation 17). To illustrate the difference between these cases, we calculate $\tau_p$ in RR1000 at room temperature with $D = 50$ $\mu$m using equations 16 and 17 for different secondary and tertiary $\gamma'$ sizes and $f_p = 0.15$, $f_s = 0.35$ and $f_t = 0.03$. Table 4 shows the microstructures considered and the predictions in both cases. For the case of lognormal size distributions, $\omega_p = 0.05$, $\omega_s = \omega_t = 0.25$ are adopted to replicate the conditions shown in the previous section. Both cases show similar predictions for all conditions, although slightly lower stresses are predicted by the model when considering lognormal size distributions. This is due to a wider size spread decreases the overall critical resolved shear stress.

The model results have been tested mostly in powder metallurgy superalloys with grain size up to 55 $\mu$m for subsolvus and supersolvus heat treatments. However, for alloys processed by the cast and wrought route (C&W), the supersolvus heat treatment can lead to grain sizes as large as 1 mm [33]. A Hall–Petch constant of 710 MPa $\mu$m$^{1/2}$ was considered in our model, although this value could differ for other conditions since there is a concomitant alteration in the $\gamma$' microstructure when modifying the grain size. In order to test the fidelity of the model for coarser grains, the yield stress in (C&W)

720Li is predicted and compared with the experimental observations from Vaunois *et al.* [33]. These alloys followed solution heat treatments at three different temperatures (1080 °C, 1120 °C and 1160 °C) in order to get different grain sizes. We consider the microstructures for the tests where oil quench was employed at the end of the solutioning treatment. The samples then were aged at 650 °C for 24 hours and followed air quenching. For the case of 1120 °C, an additional ageing step of 760 °C for 16 hours was reported. Table 3 shows the microstructures and the values of the measured yield stress for these conditions. It is worth noting that $d_t$ was not reported for the case of solutioning at 1160 °C and $d_t = 15$ nm is adopted to be consistent with similar conditions reported in their work. $\omega_p = 0.05$, $\omega_s = \omega_t = 0.25$ were considered for the particle size distributions. Our predictions show good agreement for the case of 1080 °C and 1160 °C, where $D = 4.8$ $\mu$m and 456 $\mu$m, respectively, and it underpredicts $\sigma_Y$ by 100 MPa at 1120 °C. The latter can be due to tertiary $\gamma$' not being fully dissolved and very fine particles could be aiding in increasing the precipitation strengthening term. Although the model shows good agreement, further work should be considered in C&W alloys to study the effect of microstructural inhomogenenities and coarser grains in $\sigma_Y$. These features would affect the size distribution function and number density of $\gamma'$ per grain and the Hall–Petch strengthening term.

### 7.1 Is the yield stress optimal?

From our model, it is possible to assess whether or not the microstructure adopted in these alloys provides the highest strength consistent with good creep and fatigue properties. We take $\sigma_Y$ in RR1000 at 650 °C and $D = 10$ $\mu$m as a reference case. To explore optimal microstructures for yield stress we base our analysis on two simple guidelines. 1) If the creep life is not critical, a minimum volume fraction of primary $\gamma'$ should be present in order to avoid grain growth and guarantee a fine grain microstructure [5, 32]; we then fix $f_p = 10\%$ and the remaining volume fraction is shared between secondary and tertiary $\gamma' \approx 45$ %, *i.e.* $f_s + f_t = 45$ %. 2) Combined distributions of tertiary and secondary $\gamma'$ have been shown to be beneficial for ductility, fatigue and creep properties and their effect on $\sigma_Y$ can be assessed with our model. Contour plots on the volume fraction and mean

radius effects in $\sigma_Y$ are shown in Figure 9 for (a) tertiary ($f_t$ VS $r_t$) and (b) secondary $\gamma'$ ($f_s$ VS $r_s$); the contour lines represent the conditions for iso–yield stress. In order to simplify the 4–dimensional analysis, the mean radius of secondary and tertiary $\gamma'$ were fixed in (a) and (b), respectively, and only their relative volume fraction was allowed to change. On one hand, in Fig 9(a), the maximum stress is obtained when $r_t = 10 - 15$ nm, and only marginal gains are observed when the tertiary $\gamma'$ increases when $f_t \geq 10$ %; on the other hand, in (b) the yield stress is higher as the secondary $\gamma'$ volume fraction decreases (as the tertiary $\gamma'$ volume fraction increases), although the stress increments are also marginal; coarser $\gamma'$ also shows marginal increments in $\sigma_Y$ since the relative number of tertiary $\gamma'$ ($w_t = N_t/N$) increases as the secondary $\gamma'$ radius increases for a fixed volume fraction. This shows that the tertiary $\gamma'$ size and volume fraction are the most important parameters to control, and optimal strengths ($\geq$ 1100 MPa) can be obtained as long as $f_t \geq 10$ % and $r_t = 15$ nm; the size of secondary $\gamma'$ can then be tailored to give optimal fatigue and creep properties, since the tradeoff in the yield stress is minimal [3,34]. Additionally, Crudden *et al.* [35] have pointed out that an efficient strategy for increasing the strength in superalloys is by modifying alloy composition to increase fault energies associated with anti-phase boundaries and stacking faults. Following this concept, Figure 9(c) shows a parametric analysis on the effects of $\gamma_{APB}$ and the $\gamma'$ volume fraction in $\sigma_Y$ for alloys sustaining unimodal size distributions and (d) for alloys having multimodal $\gamma'$ size distributions consistent with the previous design criteria (fixed $f_p = 10\%$, $r_p = 500$ nm, $r_s = 100$ nm, $f_t = 10$ % and $r_t = 15$ nm); the shadowed bands show the range of $\gamma_{APB}$ values in commercial superalloys [35]. A fixed solid solution contribution is assumed (from the RR1000 base composition) in the calculations for simplicity. The total $\gamma'$ volume variation is displayed in (d), although only $f_s$ is changing, *i.e.* $f_s = 0$ for $f < 20\%$ and it only increases above this value. The yield stress can reach 1800 MPa if the antiphase boundary energy increases up to 0.5 J/m$^2$ and $f > 40\%$ in the unimodal alloy, whereas it peaks at $\sim$ 1650 MPa for the multimodal distribution with the same APB energy and volume fraction. This implies that a 150 MPa tradeoff in $\sigma_Y$ is to be expected for assuring good mechanical properties (ductility, creep and fatigue life), although these values are

higher for higher $\gamma_{APB}$. These results illustrate how the model can be employed as a tool for process and alloy design. However, it is important to remark that variations in $\gamma_{APB}$ can also affect the lattice misfit and $\gamma'$ volume fraction, and this should be considered more in detail.

## 7 Conclusions

The following conclusions can be outlined from this work:

- A unified description of precipitation shear strengthening in alloys with unimodal and multimodal particle size distributions was described by revisiting the classic models on weak and strong pair–coupling.
- An intermediate dislocation pair–coupling configuration was shown to link the classic weak and strong pair models and accurately describe the transition range where maximum strength occurs.
- It was verified theoretically that the yield stress is higher for alloys with unimodal $\gamma'$ sizes compared to their counterpart with a multimodal size distribution. This results from the strength being distributed according to the relative particle number.
- It was shown that the tertiary $\gamma'$ size and volume fraction are the main microstructural parameters controlling the strength of alloys multimodal distributions.
- The relative contribution of each strengthening mechanism was deconvoluted in polycrystalline superalloys. This allowed us identify the terms contributing to the strength loss found between supersolvus and subsolvus heat–treatments.

## Acknowledgements

The authors would like to acknowledge the EPSRC (grants EP/H022309/1, EP/H500375/1) and Rolls-Royce plc. for funding and Prof. Mark Blamire for provision of facilities. Requests for access to the underlying research data should be directed to the corresponding author and will be considered against commercial interests and data protection.

## Appendix

The atom fraction of each alloying element in the $\gamma$ and its solid solution constant ($\beta_i$) are needed to estimate $\sigma_{ss}$ in the yield stress equation. The atom fraction in the matrix was directly obtained from the experiments for IN 100 [14] and in RR1000 [6]; Thermocalc was employed in the other alloys, where for the case of Mo, Cr and other elements forming other secondary phases such as $\sigma$ were assumed to fully partition in the matrix [36]. Table 5 shows the atom fraction $x_i$ for these alloys. The values of $\beta_i$ calculated with the expressions introduced in Section 4 are also shown in this table (including $\eta_i'$ and $\delta_i$), as well as the shear modulus $\mu_i$ and atomic radius $r_i^a$ values of each alloying element. They were obtained from [37]; $\mu_{Ni} = 80$ GPa and $r_{Ni}^a = 0.117$ nm were adopted for simplicity in the calculations. By the definition of $\beta_i$, the lattice misfit $\delta_i$ displays stronger effect than $\eta_i'$ and higher strengthening is predicted for alloying elements with large atomic radius, such as Mo, Nb, Ta, Ti, and W, whereas low strengthening occurs in elements with smaller $r_i^a$, such as Al, Co and Cr; modulus distortion effects in strengthening are significantly lower. Additionally, the values of $\beta_i$ are compared with those experimentally estimated by Roth *et al.* [38] in multicomponent Ni alloys[‡‡]; this work extends the earlier results by Mishima *et al.* [39] estimating $\beta_i$ for binary Ni alloys at 77 K. Roth *et al.* and our $\beta_i$ values are very similar in Cr, Co, Mo and Al, whilst our predictions display higher values in W, Ti, Ta and Nb. These discrepancies can be due to the difference in the exponents considered by Roth *et al.*, as the results originally obtained by Mishima *et al.* showed that W, Nb and Ta have much higher contribution than Mo and Ti has a similar strengthening coefficient than Mo. Our results are consistent with Mishima *et al.* observations.

# References

[1] R. Reed, The superalloys: Fundamentals and applications, Cambridge University Press, Cambridge, 2006.

[‡‡] They estimated solid solution hardening using different exponents: $\left(\sum \beta_i^2 x_i\right)^{1/2}$. Nevertheless, our predictions and their values are consistent, as the exponents only affect the atom fraction, since $\beta_i$ accounts for the strengthening contribution of the binary system.

[2] R. Unocic, G. Viswanathan, P. Sarosi, S. Karthikeyan, J. Li, M. Mills, Mechanisms of creep deformation in polycrystalline Ni-base disk superalloys, Mater. Sci. Eng. A 483 (2008) 25–32.

[3] J. Telesman, P. Kantzos, J. Gayda, P. Bonacuse, A. Prescenzi, Microstructural variable controlling time-dependent crack growth in a P/M superalloy, Superalloys (2004) 215–224.

[4] J. Telesman, T. Gabb, A. Garg, P. Bonacuse, J. Gayda, Effect of microstructure on time dependent fatigue crack growth behaviour in a P/M turbine disk alloy, Superalloys (2008) 807–816.

[5] D. Collins, H. Stone, A modelling approach to yield strength optimisation in a nickel-base superalloy, Int. J. Plast. 54 (2014) 96–112.

[6] L. Connor, The development of a dual microstructure heat treated Ni-base superalloy for turbine disc applications, Ph.D. thesis, University of Cambridge (2009).

[7] L. Brown, R. Ham, in Strengthening methods in crystals by Kelly and Nicholson, Elsevier, Oxford, 1971.

[8] D. Raynor, J. Silcock, Strengthening mechanisms in $\gamma'$-precipitating alloys, Metal Sci. J. 4 (1970) 121.

[9] B. Reppich, Some new aspects concerning particle hardening mechanisms in $\gamma'$ precipitating Ni-base alloys–I. Theoretical concept, Acta Metall. 30 (1982) 87–94.

[10] B. Reppich, P. Schepp, G. Wehner, Some new aspects concerning particle hardening mechanisms in $\gamma'$ precipitating Ni-base alloys–II. Experiments, Acta Metall. 30 (1982) 95–104.

[11] A. Ardell, Precipitation hardening, Metall. Trans. A 16 (1985) 2131–2165.

[12] E. Nembach, G. Neite, Precipitation hardening of superalloys by ordered $\gamma'$-particles, Prog. Mater. Sci. 29 (1985) 177–319.

[13] Reppich, B. In: Cahn RW, Haasen P, Kramer RT. Materials Science and Technology, Plastic deformation and fracture, Vol. 6, Wiley-VCH, 1993.

[14] R. Kozar, A. Suzuki, W. Milligan, J. Schirra, M. Savage, T. Pollock, Strengthening mechanisms in polycrystalline multimodal nickel-base superalloys, Metall. Mater. Trans. A 40 (2009) 1588–1603.

[15] M. Jackson, R. Reed, Heat treatment of UDIMET 720Li: the effect of microstructure on properties, Mater. Sci. Eng. A 259 (1999) 85–97.

[16] J. Friedel, Dislocations, Addison-Wesley, Reading, 1964.

[17] A. Ardell, V. Munjal, D. Chellman, Precipitation hardening of Ni-Al alloys containing large volume fractions of $\gamma'$, Metall. Trans. A 7 (1976) 1263–1268.

[18] E. Nembach, S. Schänzer, W. Schröer, Trinckauf, Hardening of nickel-base superalloys by high volume fractions of $\gamma'$-precipitates, Acta Metall. 36 (1988) 1471–1479.

[19] J. Coakley, D. Dye, H. Basoalto, Creep and creep modelling of a multimodal nickel-base superalloy, Acta Mater. 59 (2011) 854–863.

[20] A. Sequeira, H. Calderon, G. Kostorz, J. Pedersen, Bimodal size distributions of $\gamma'$ precipitates in Ni-Al-Mo–II. transmission electron microscopy, Acta Metall. Mater. 43 (1995) 3441–3439.

[21] T. Osada, N. Nagashima, Y. Gu, Y. Yuan, T. Yokokawa, H. Harada, Factors contributing to the strength of a polycrystalline nickel-cobalt base superalloy, Scripta Mater. 64 (2011) 892–895.

[22] U. Kocks, H. Mecking, Physics and phenomenology of strain hardening: the FCC case, Prog. Mater. Sci. 48 (2003) 171–273.

[23] R. Labusch, A statistical theory of solid solution hardening, Phys. Stat. Sol. 41 (1970) 659–669.

[24] L. Gypen, A. Deruyttere, Multi-component solid solution hardening: Part 1 proposed model, J. Mater. Sci. 12 (1977) 1028–1033.

[25] L. Gypen, A. Deruyttere, Multi-component solid solution hardening: Part 2 agreement with experimental results, J. Mater. Sci. 12 (1977) 1034–1038.

[26] R. Fleischer, Substitutional solution hardening, Acta Metall. 11 (1963) 203–209.

[27] T. Kruml, B. Viguer, J. Bonnevile, J. Martin, Temperature dependence of dislocation microstructure in $Ni_3$(Al,Hf), Mater. Sci. Eng. A 234 (1997) 755–757.

[28] D. Dye, J. Coakley, V. Vorontsov, H. Stone, R. Rogge, Elastic moduli and load partitioning in a single-crystal nickel superalloy, Scripta Mater. 61 (2009) 109–112.

[29] B. Grant, H. Stone, P. Withers, M. Preuss, High-temperature strain field measurement using digital image correlation, J Strain Analysis 44 (2009) 263–271.

[30] J. He, G. Han, S. Fukuyama, K. Yokogawa, Interfaces in a modified Inconel 718 with compact precipitates, Acta Mater. 46 (1998) 215–223.

[31] K. Gopinath, A. Gogia, S. Kamat, R. Balamuralikrishnan, U. Ramamurty, Tensile properties of Ni–Based superalloy 720Li: temperature and strain rate effects, Metall. Mater. Trans. A 39 (2008) 2340–2350.

[32] R. Mitchell, J. Lemsky, R. Ramanathan, H. Li, K. Perkins, L. Connor, Process development & microstructure & mechanical properties of a dual microstructure heat treated advanced nickel disk alloy, Superalloys (2008) 347–356.

[33] J. Vanouis, J. Cormier, P. Villechaize, A. Devaux, B. Flageolet, Influence of both $\gamma'$ distribution and grain size on the tensile properties of UDIMET 720Li at room temperature, Superalloys 718 and derivatives (2010) 199–213.

[34] G. Viswanathan, P. Sarosi, M. Henry, D. Whitis, W. Milligan, M. Mills, Investigation of creep deformation mechanisms at intermediate temperatures in René 88 DT, Acta Mater. 53 (2005) 3041–3057.

[35] D. Crudden, A. Mottura, N. Warnken, B. Raeisinia, R. Reed, Modelling of the influence of alloy composition on flow stress in high-strength nickel-based superalloys, Acta Mater. 75 (2014) 356–370.

[36] R. Reed, M. Jackson, Y. Na, Characterization and modelling of the precipitation of the sigma phase in UDIMET 720 and UDIMET 720Li, Metall. Mater. Trans. A 30 (1999) 521–533.

[37] D. Lide, CRC Handbook of Chemistry and Physics, CRC Press, 2008.

[38] H. Roth, C. Davis, R. Thomson, Modeling solid solution strengthening in nickel alloys, Metall. Trans. A 28 (1997) 1329–1335.

[39] Y. Mishima, S. Ochiai, N. Hamao, M. Yodogawa, T. Suzuki, Solid solution hardening of nickel - role of transition metal and B-subgroup solutes -, T. Jpn. I. Met. 27 (1986) 656–664.

[40] M. Ahmadi, E. Povoden-Karadeniz, L. Whitmore, M. Stockinger, A. Falahati, E. Kozeschnik, Yield strength prediction in Ni-base alloy 718Plus based on thermo-kinetic precipitation simulation, Mater. Sci. Eng. A 608 (2014) 114–122.

[41] S. Sinharoy, P. Virro-Nic, W. Milligan, Deformation and strength behavior of two nickel-base turbine disk alloys at 650°C, Metall. Mater. Trans. A 32 (2001) 2021–2032.

Table 1: Chemical composition and strengthening particle volume fraction of the superalloys tested in this work.

| Alloy | Ni | Cr | Co | Mo | W | Al | Ti | Ta | Nb | $f$ (%) |
|---|---|---|---|---|---|---|---|---|---|---|
| ATI 718Plus | Bal. | 17.42 | 9.13 | 2.72 | 1.04 | 1.46 | 0.71 | – | 5.48 | 14–18 |
| KM4 | Bal. | 12 | 18 | 4 | – | 4 | 4 | – | 2 | 55 |
| IN100 | Bal. | 12.3 | 18.3 | 3.3 | – | 4.9 | 4.3 | – | – | 60 |
| RR1000 | Bal. | 15 | 18.5 | 5 | – | 3 | 3.6 | 2 | 1.1 | 40–55 |
| Udimet 720Li | Bal. | 16 | 15 | 3 | 1.25 | 2.5 | 5 | – | – | 45–50 |

Table 2: Initial microstructures of the superalloys tested. Uni, Sub and Sup stand for unimodal $\gamma'$, subsolvus and supersolvus heat treatment, respectively.

| Alloy | $D$ ($\mu$m) | $f_p$ (%) | $r_p$ (nm) | $f_s$ (%) | $r_s$ (nm) | $f_t$ (%) | $r_t$ (nm) | Ref. |
|---|---|---|---|---|---|---|---|---|
| ATI 718Plus | 20 | – | – | 14–19 | 7– 26 | – | – | [40] |
| KM4 (Uni) | 6 | – | – | 55 | 50–340 | – | – | [41] |
| KM4 (Sub) | 6 | 11 | 1000 | 35 | 145 | 9 | 35 | [41] |
| KM4 (Sup) | 55 | – | – | 45 | 180 | 10 | 20 | [41] |
| IN100 (Sub) | 4.1 | 20 | 600 | 34 | 85 | 6 | 4 | [14] |
| IN100 (Sup) | 34.4 | – | – | 46 | 170 | 14 | 5.5 | [14] |
| RR1000 | 7–46 | 0–12 | 408–765 | 36–43 | 91–114 | 1–3 | 8.8–11 | [6] |
| 720Li (Sub) | 10 | 15 | 750 | 27 | 55, 60 | 3 | 21, 30 | [15] |
| 720Li (Sup) | 30 | 10 | 750 | 39 | 57 | 1 | 15 | [15] |
| 720Li | 11 | 18 | 750 | 22 | 55 | 5 | 15 | [31] |

Table 3: Model comparison with experiments in 720Li for wide grain size ranges. Exp. and Mod. stand for the measured and predicted yield stress, respectively.

| Sol. Temp (°C) | 1080 | 1120 | 1160 |
|---|---|---|---|
| $D$ ($\mu$m) | 4.8 | 12.9 | 456 |
| $f_p$ (%) | 18 | 14.1 | 0.1 |
| $d_p$ (nm) | 1670 | 2230 | 2110 |
| $f_s$ (%) | 9.2 | 30.9 | 20 |
| $d_s$ (nm) | 233 | 35.4 | 55 |
| $f_t$ (%) | 17.8 | - | 24.9 |
| $d_t$ (nm) | 14.3 | - | 15 |
| Exp. $\sigma_Y$ (MPa) | 1224 | 1250 | 955 |
| Mod. $\sigma_Y$ (MPa) | 1210 | 1154 | 931 |

Table 4: Comparison in $\tau_p$ when considering lognormal size distributions and only mean radii.

| Case | $r_s$ (nm) | $r_t$ (nm) | $\tau_p$ (MPa) | $r_s$ (nm) | $r_t$ (nm) | $\tau_p$ (MPa) |
|---|---|---|---|---|---|---|
| Size distribution | 200 | 40 | 227 | 200 | 20 | 255 |
| Mean values | 200 | 40 | 235 | 200 | 20 | 262 |
| Size distribution | 100 | 40 | 240 | 100 | 20 | 255 |
| Mean values | 100 | 40 | 242 | 100 | 20 | 260 |

Table 5: Elemental atom fraction in the matrix and $\mu_i$ and $r_i^a$ of the respective alloying elements. $\beta_i$ calculations in this work and estimations from [38].

| Alloy | Cr | Co | Mo | W | Al | Ti | Ta | Nb |
|---|---|---|---|---|---|---|---|---|
| ATI 718Plus | 0.23 | 0.11 | 0.0246 | 0.005 | 0.0016 | 0.0003 | - | 0.03 |
| KM4 (Uni) | 0.24 | 0.3 | 0.015 | - | 0.009 | 0.0012 | - | - |
| KM4 (Sub) | 0.24 | 0.3 | 0.015 | - | 0.009 | 0.0012 | - | - |
| KM4 (Super) | 0.24 | 0.3 | 0.015 | - | 0.009 | 0.0012 | - | - |
| IN100 | 0.25 | 0.28 | 0.057 | 0.02 | 0.001 | - | - | |
| RR1000 | 0.25 | 0.25 | 0.0825 | - | 0.0086 | 0.002 | 0.0014 | - |
| Udimet 720Li | 0.3 | 0.21 | 0.02 | 0.003 | 0.005 | 0.002 | - | - |
| $\mu_i$ (GPa) | 115 | 75 | 126 | 161 | 26 | 44 | 69 | 38 |
| $r_i^a$ (nm) | 0.13 | 0.118 | 0.146 | 0.15 | 0.124 | 0.148 | 0.158 | 0.156 |
| $\eta_i'$ | 0.36 | 0.06 | 0.44 | 0.67 | 0.5 | 0.36 | 0.12 | 0.41 |
| $\delta_i$ | 0.11 | 0.008 | 0.25 | 0.28 | 0.06 | 0.26 | 0.35 | 0.33 |
| $\beta_i$ (MPa/at$^{2/3}$) | 375 | 10 | 1112 | 1417 | 212 | 1186 | 1648 | 1654 |
| $\beta_i$ (MPa/at$^{1/2}$) from [38] | 337 | 39.4 | 1015 | 977 | 225 | 775 | 1191 | 1183 |

Table 6: Nomenclature

| | |
|---|---|
| $b$ | Magnitude of the Burgers vector [m] |
| $\beta_i$ | Solid solution constant of alloying element $i$ [MPa/at$^{3/2}$] |
| $D$ | Mean grain size [$\mu$m] |
| $\delta(r)$ | Dirac delta function |
| $\delta_i$ | lattice distortion of alloying element $i$ with respect to Ni |
| $\eta_i$ | modulus distortion of alloying element $i$ with respect to Ni |
| $\eta_i'$ | constant related to $\eta_i$ |
| $f$ | Total volume fraction of $\gamma'$ |
| $f_p$, $f_s$, $f_t$ | Volume fraction of primary, secondary and tertiary $\gamma'$ |
| $\gamma_{APB}$ | Antiphase boundary energy [J/m$^2$] |
| $k_Y$ | Hall–Petch constant [MPa $\mu$m$^{1/2}$] |
| $L$ | Mean particle spacing [m] |
| $l_1$, $l_2$ | Segment length of the leading (1) and trailing (2) dislocations acting in the cutting of a particle [m] |
| $\lambda_1$ | Friedel spacing [m] |
| $\Lambda_1$, $\Lambda_2$ | Effective length of the leading (1) and trailing (2) dislocations driving particle cutting [m] |
| $\mu$ | Shear modulus [GPa] |
| $\mu_i$ | Shear modulus of the alloying element [GPa] |
| $N$ | Total particle number of $\gamma'$ |
| $N_p$, $N_s$, $N_t$ | particle number of the primary/secondary/tertiary $\gamma'$ |
| $\omega_p$, $\omega_s$, $\omega_t$ | Constant in the lognormal size distribution of the primary, secondary and tertiary $\gamma'$ |
| $p$ | Total particle size distribution in the specimen |
| $p_p$, $p_s$, $p_t$ | Individual particle size distribution of primary, secondary and tertiary $\gamma'$ |
| $r$ | mean $\gamma'$ radius (unimodal size distribution) [m] |
| $r_p$, $r_s$, $r_t$ | mean radius of primary, secondary and tertiary $\gamma'$ [m] |

Table 7: Nomenclature (cont.)

| | |
|---|---|
| $r_i^a$ | atomic radius of alloying element $i$ [nm] |
| $r_{Ni}^a$ | atomic radius of Ni [nm] |
| $r_m$ | particle radius with maximum strength [m] |
| $\sigma_Y$ | Yield stress [MPa] |
| $\sigma_p$ | Precipitation shearing stress [MPa] |
| $\sigma_{Oro}$ | Orowan axial stress [MPa] |
| $\sigma_{ss}$ | Solid solution strengthening [MPa] |
| $\sigma_D$ | Hall–Petch strengthening [MPa] |
| $\tau_p$ | Critical resolved shear stress for cutting a particle [MPa] |
| $\tau_{Oro}$ | Orowan shear stress [MPa] |
| $w_p$, $w_s$, $w_t$ | particle number fraction of primary, secondary and tertiary $\gamma'$ |

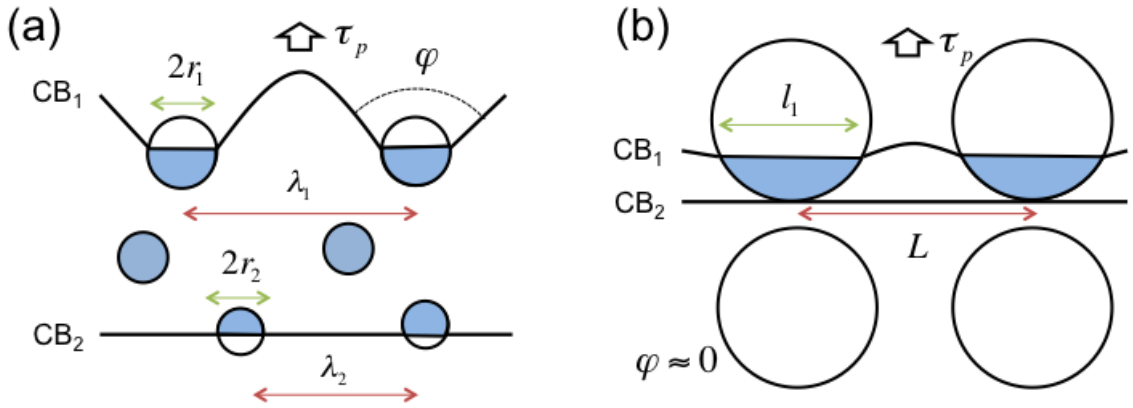


Figure 1: Schematic illustrations of the dislocation configurations in the case of (a) weak pair–coupling and (b) strong pair–coupling. The shadowed regions represent the area sheared by the leading dislocation.

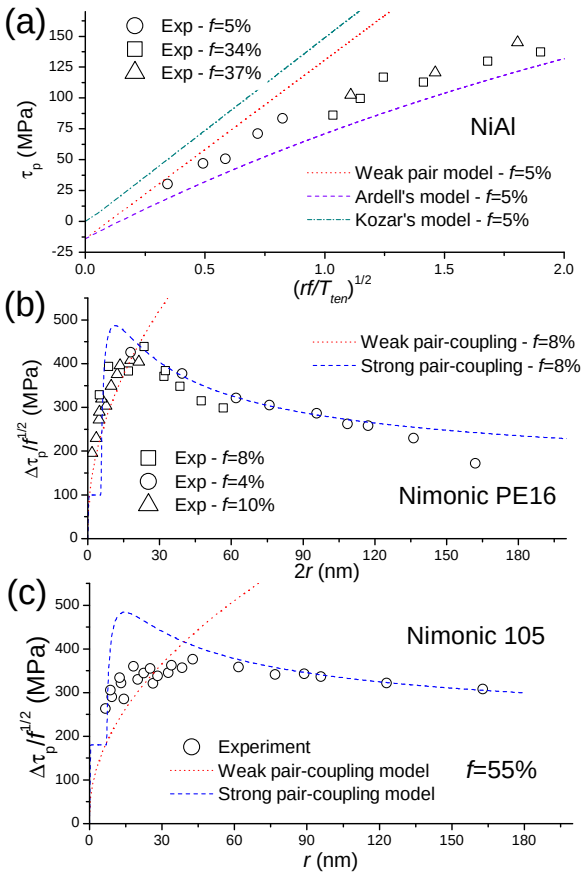


Figure 2: Predictions of the room–temperature critical resolved shear stress due to particle shear in (a) NiAl employing the weak pair–coupling, Kozar and Ardell's models. Additional predictions of the resolved shear stress in (b) Nimonic PE16 and (c) Nimonic 105 employing the weak and strong pair–coupling models.

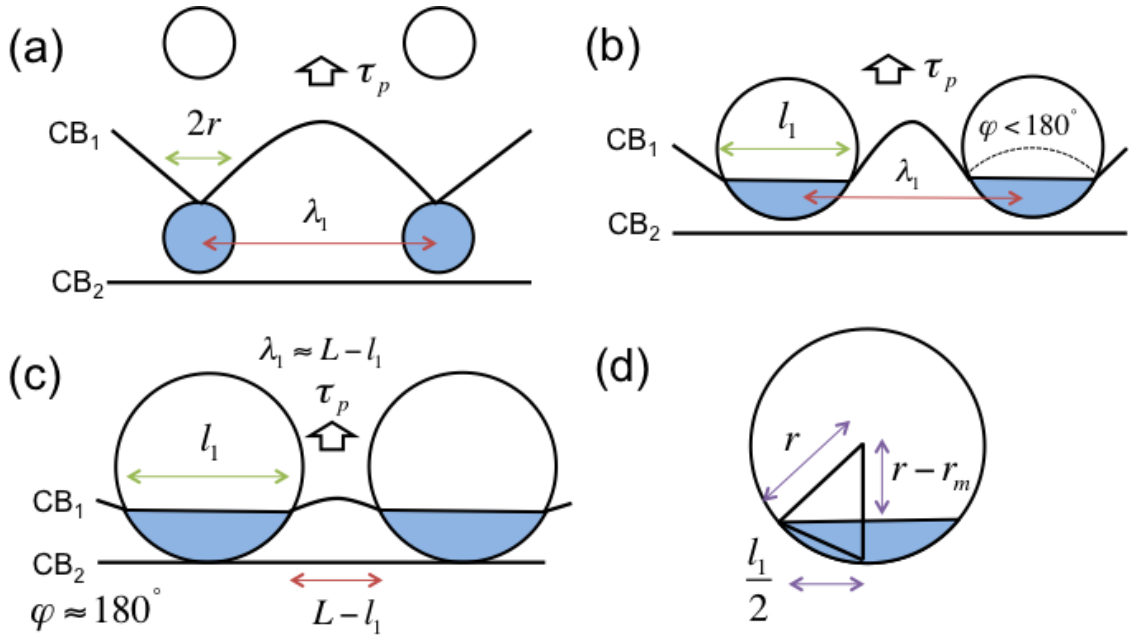


Figure 3: Schematic illustration of the modified dislocation configurations in the case of (a) weak pair–coupling, (b) intermediate pair–coupling and (c) strong pair–coupling. (d) Schematic representation of the geometric configuration between $l_1$, $r$ and $r_m$ in the case of partial shear.

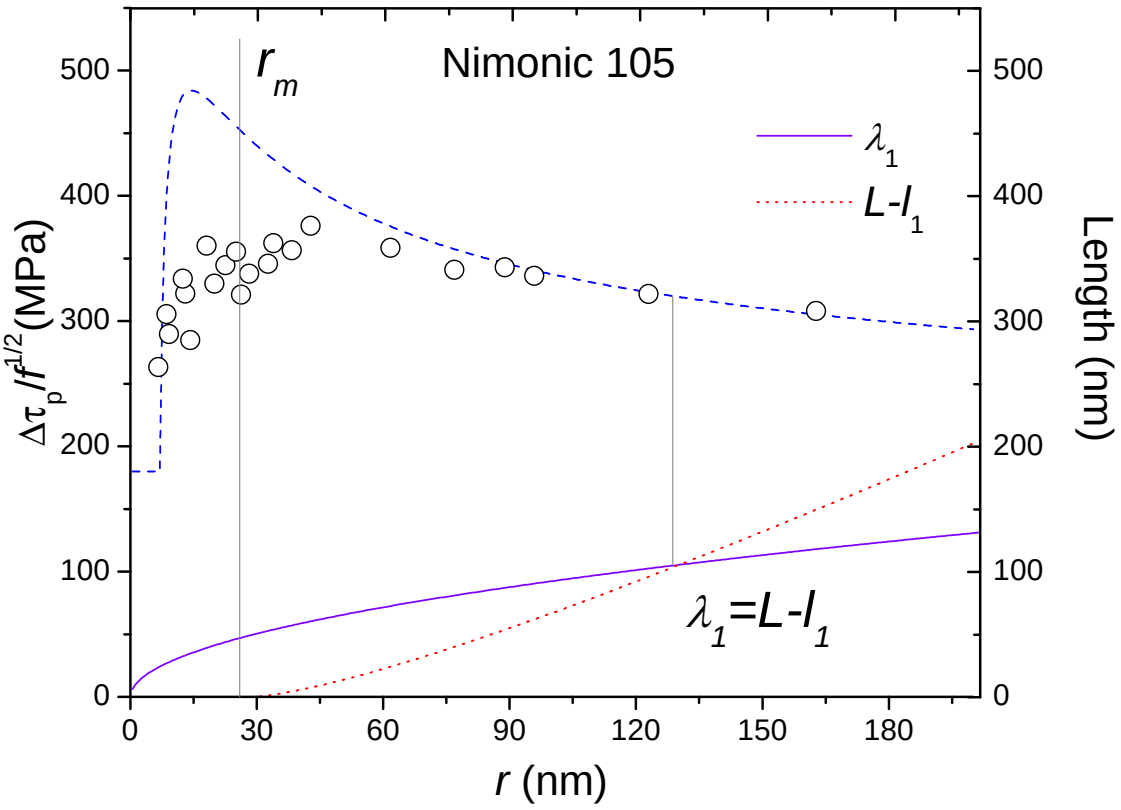


Figure 4: Variation in the effective length being sampled by a bowing/straight dislocation and its effect on the resolved shear stress in Nimonic 105. The dashed line represent the critical resolved shear stress predicted by the strong pair model.

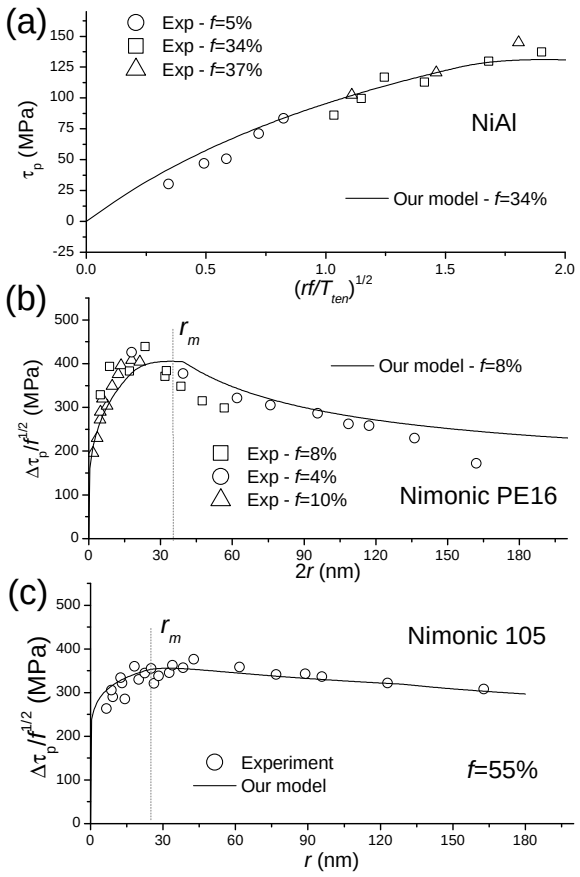


Figure 5: Our predictions of the room–temperature critical resolved shear stress due to particle shear in (a) NiAl, (b) Nimonic PE16 and (c) Nimonic 105.

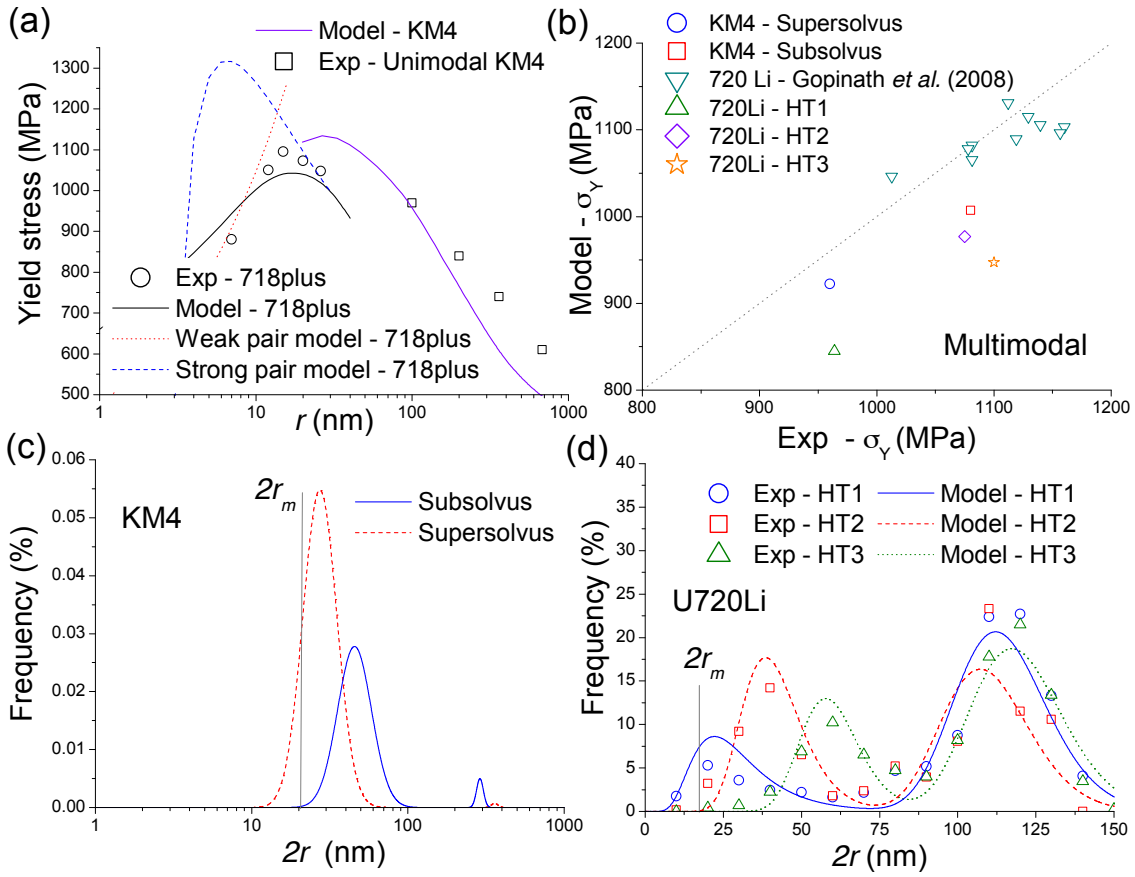


Figure 6: Model comparison with experimental measurements on the yield stress for superalloys with (a) unimodal and (b) multimodal $\gamma'$ size distributions. The particle size distributions in KM4 and 720Li (HT1–3) are shown in (c) and (d), respectively.

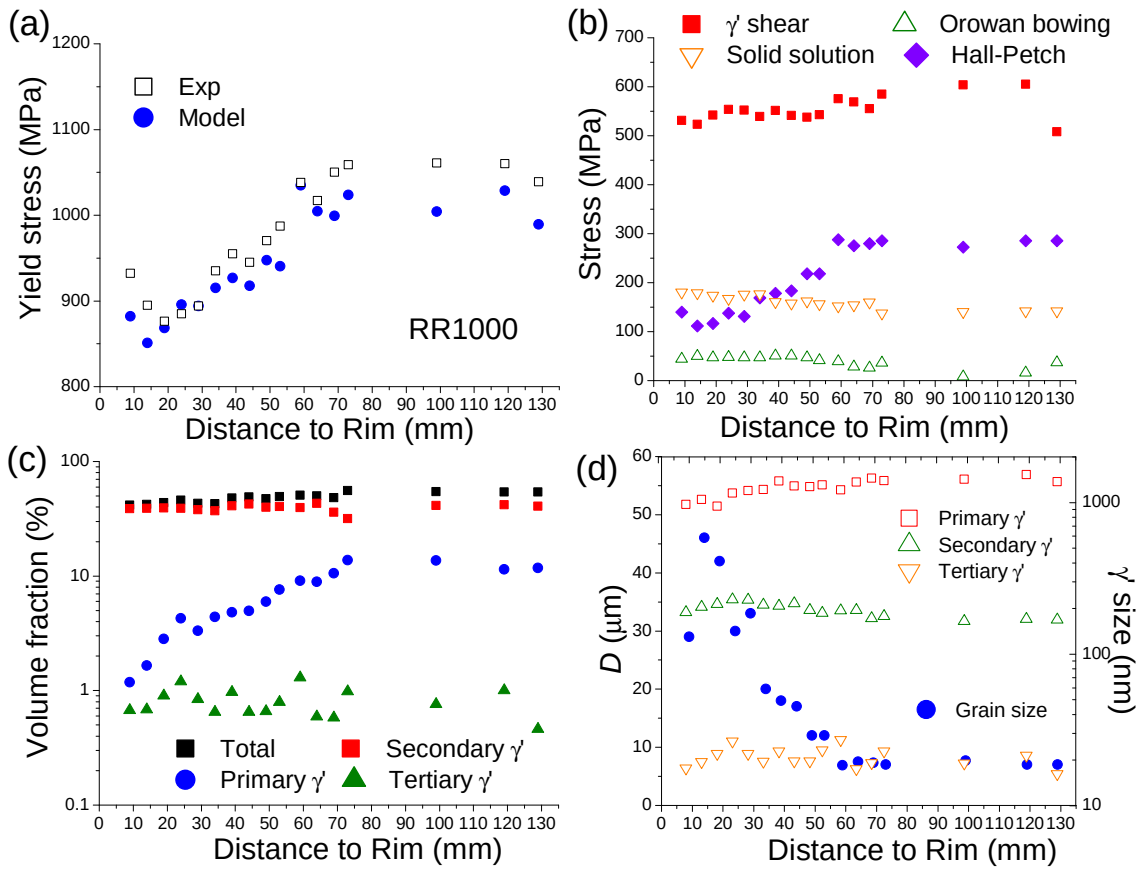


Figure 7: Strength and microstructure characterisation in RR1000 under dual microstructure heat treatment (DMHT) [6, 32]. (a) Yield stress predictions and measurements, (b) model estimation of the individual contributions to the total strength; experimental (c) $\gamma'$ volume fraction characterisation and (d) grain size and $\gamma'$ mean size; all the experiments are expressed as a function of the distance from the bore to the rim of a turbine disk.

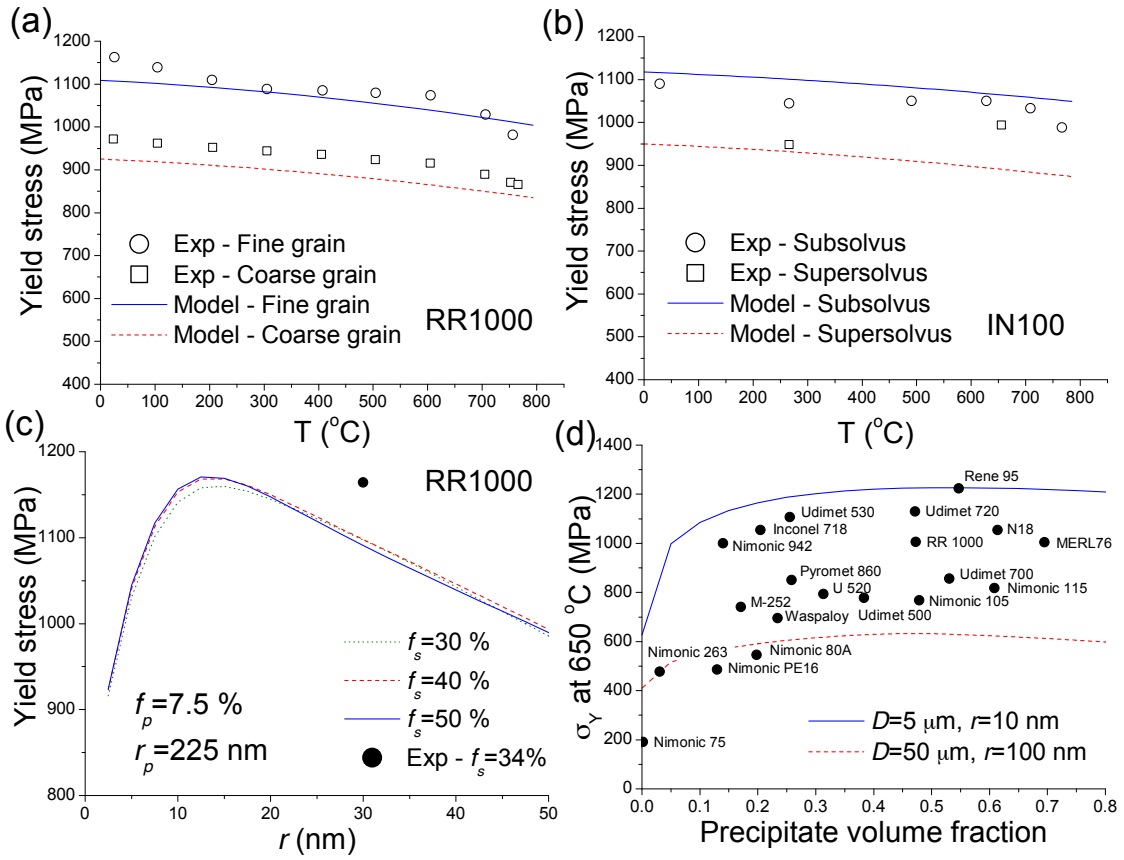


Figure 8: Temperature effects on the yield stress in (a) RR1000 and (b) IN100. (c) Yield stress in RR1000 with unimodal $\gamma'$ size at different volume fractions. (d) Model predictions at 650 °C in fine and coarse microstructures for different precipitate volume fractions and $\sigma_Y$ values in number of common precipitation–strengthened superalloys.

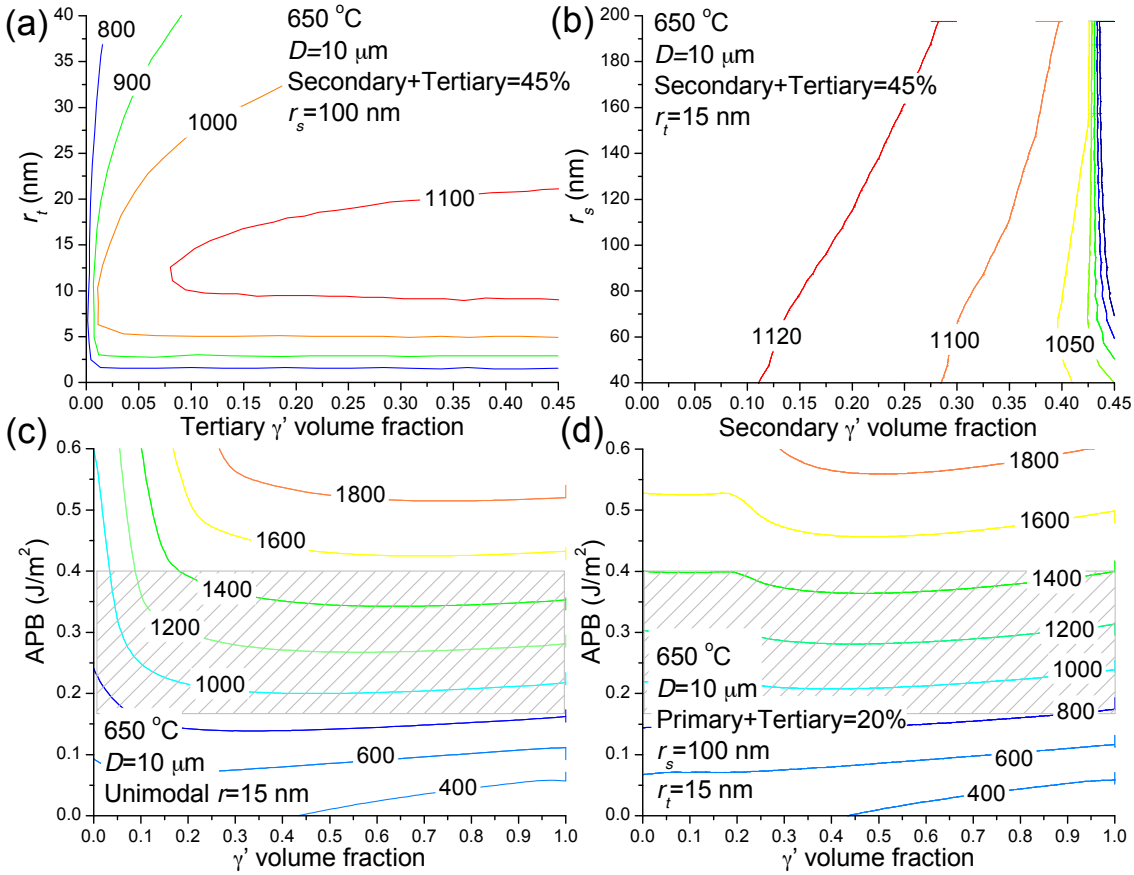


Figure 9: Parametric analysis on the various parameters affecting the yield stress in RR1000 for different (a) tertiary and (b) secondary $\gamma'$ conditions. Yield stress evolution as a function of the antiphase boundary energy and $\gamma'$ volume fraction with (c) unimodal and (d) multimodal size distributions. The shadowed bands show the range of $\gamma_{APB}$ values in commercial superalloys